

# In search of Covalent Organic Framework photocatalysts: A DFT-based screening approach

Beatriz Mourino, Kevin Maik Jablonka, Andres Ortega-Guerrero,\* and Berend Smit\*

*Laboratory of Molecular Simulation (LSMO), Institut des Sciences et Ingénierie Chimiques, Ecole Polytechnique Fédérale de Lausanne (EPFL), Rue de l'Industrie 17, CH-1951 Sion, Valais, Switzerland*

E-mail: oandresg15@gmail.com; berend.smit@epfl.ch

## Abstract

Covalent organic frameworks (COFs) stand out as prospective organic-based photocatalysts given their intriguing optoelectronic properties, such as visible light absorption and high charge-carrier mobility. The CURATED COFs is a database of reported experimental COFs that until now remained mostly unexplored for photocatalysis. In this work, we screen the CURATED COFs database for discovering potential photocatalysts using a set of DFT-based descriptors that cost-effectively assesses visible light absorption, preliminary thermodynamic feasibility of the desired pair of redox reactions, charge separation, and charge-carrier mobility. The workflow can shortlist 13 COFs as prospective candidates for water splitting, and identify materials ( $N_x$ -COF ( $x = 0-3$ )) that have been reported as candidates for Hydrogen evolution reaction (HER). Overall, our strategy tackles the challenge of having too many COFs to explore by channeling the focus of future research to a selective group of COFs while elucidating insights into the structure design for a desired photocatalytic process.

## 15 Introduction

16 Photocatalysis offers a pathway for green energy and chemical industry alternatives such  
17 as sunlight-driven water splitting and CO<sub>2</sub> reduction. In such processes, solar-to-chemical  
18 energy conversion provides the driving force to generate renewable fuels and chemicals as a  
19 promising solution to the energy and environmental crisis. In short, vastly available sunlight  
20 in a photocatalytic system is absorbed, followed by photo-generation of separated charge  
21 carriers in the material valence (VB) and conduction (CB) bands. These charge carriers can  
22 participate in the desired surface reactions.<sup>1,2</sup>

23 Whether the promise of a photocatalysis-based sustainable future can reach industrial  
24 plants strongly depends on finding a material that can optimally fulfill requirements for each  
25 step of a photocatalytic process. An ideal photocatalyst should have valence and conduction  
26 band edges straddling the potentials of the targeted redox reactions, should absorb visible light,  
27 display high charge-carrier mobility, and have low detrimental electron-hole recombination.  
28 Covalent organic frameworks (COFs) stand out given their modular nature, optoelectronic  
29 properties, and stability. COFs are porous crystalline materials composed predominantly  
30 of earth-abundant, non-toxic elements and based on the connection of building blocks, *i.e.*  
31 linkers and linkages, through reversible covalent bonds.<sup>3,4</sup> Most COFs are layered materials  
32 of two-dimensional (2D) sheets, commonly referred to as 2D COFs,<sup>5</sup> displaying mechanical,  
33 optical, and electronic properties that can be extremely advantageous for photocatalytic  
34 properties, such as visible light absorption and high charge-carrier mobility.<sup>6</sup> Many COFs  
35 possess large surface areas, functional group tunability, and solution processability. The  
36 combination of such properties permits an unlimited number of functionality-based designed  
37 materials. Due to the above-mentioned advantages, there is an increasing interest in using  
38 COFs and their composites as photocatalysts in overall water splitting, H<sub>2</sub> generation, CO<sub>2</sub>  
39 reduction, and degradation of organic pollutants.<sup>7,8</sup>

40 Interestingly, a simple literature search in the Web of Science database (filtered for the  
41 keywords “Covalent organic framework” or “COF” and “photocatalysis” or “photocatalyst”)

42 shows that to this moment, about 90% of the experimental COFs originally queried for  
43 this work remain unexplored for photocatalysis. Given a large number of already synthe-  
44 sized COFs,<sup>9</sup> computational screening approaches can aid the exploration of properties and  
45 structure-property relationships by quickly surveying many variables, thus redirecting experi-  
46 mental efforts.<sup>10</sup> Here, we developed a high-throughput density functional theory (DFT)-based  
47 workflow to discover photocatalytically active COFs. The strategy behind our workflow is to  
48 implement cost-effective DFT calculations enabling us to discover materials of interest given  
49 a high number of COFs structures. Our methodology defines a set of descriptors to evaluate  
50 the material’s performance in the fundamental steps of photocatalysis. The descriptors are  
51 obtained through post-processing of DFT outputs to properly assess photocatalysis-specific  
52 features associated with the material’s performance. The screening workflow takes as in-  
53 put the “Clean, Uniform, Refined with Automatic Tracking from Experimental Database”  
54 (CURATED) COFs,<sup>11</sup> a database of reported experimental COFs.

## 55 **Screening strategy**

56 With a defined set of materials to be evaluated, developing a thorough strategy is crucial as  
57 it will dictate the accuracy and feasibility of the screening protocol. The strategy employed  
58 in this work focuses on 1) determining DFT descriptors for the fundamental steps of a  
59 photocatalytic process and the approximations to be employed and 2) establishing a cost-  
60 effective way to compute those descriptors.

61 **Photocatalytic DFT descriptors** Firstly, we determine DFT-based descriptors of the  
62 photocatalytic steps considering a strategy that enables us to obtain satisfactory yet cost-  
63 effective results for a screening study. In this work, the selected descriptors are the following:  
64 1) energy-based descriptors, *i.e.* band gap and band-edge alignment to the redox reactions  
65 to assess visible-light absorption and thermodynamics, respectively, 2) a charge separation  
66 descriptor, and 3) a charge-carrier mobility descriptor to assess the performance of the

67 material.

68 **Energy-based descriptors** The thermodynamic feasibility of a photo-redox reaction  
69 can be evaluated by ionization potential (IP) and electron affinity (EA) values. The IP  
70 can be associated with the absolute energy of the valence band edge after alignment with  
71 a reference level. The EA is taken to be the difference between the IP and the band  
72 gap.<sup>12,13</sup> This association is an approximation since Kohn-Sham energy levels are affected by  
73 the derivative discontinuity where common density functional approximations (Generalized  
74 gradient approximation (GGA), Meta-GGA, and Hybrids) differ from experimental values.<sup>12,14</sup>  
75 The reference level can be estimated by determining the vacuum potential in the pores where  
76 the variation of the electrostatic potential is the smallest, similar to what has been previously  
77 reported for MOFs and COFs.<sup>15,16</sup> The obtained absolute energies of IP and EA can then  
78 be used to select materials whose band edges align with the target redox potentials of the  
79 desired reactions, all referenced to vacuum. Hence, in this way, we ensure the thermodynamic  
80 feasibility of the desired reaction. In the case of hydrogen (HER) and oxygen (OER) evolution  
81 reactions, the redox potentials at pH 0 are  $-4.4\text{ eV}$  and  $-5.63\text{ eV}$  aligned to the vacuum  
82 level,<sup>17</sup> respectively.

83 To evaluate visible-light absorption, the Kohn-Sham band gap is calculated and empirically  
84 adjusted to PBE0 values, as discussed in the following section. Ideally, computational  
85 determination of the optical band gap should rely on methods that account for the excited  
86 states, especially for organic materials where excitonic effects are important.<sup>12,18,19</sup> However,  
87 some hybrid functionals, such as PBE0, can be reasonably accurate for some systems when  
88 calculating the optical band gap; and an empirical adjustment of PBE to PBE0 values  
89 employed here is justified by its cost-effectiveness. Hybrid functionals are particularly  
90 accurate in predicting optical band gaps when no charge transfer excitation is involved.<sup>20</sup>

91 **Charge separation descriptor** The exciton generated by light absorption can then  
92 undergo the process of charge separation (independent charge carriers, *i.e.* electron and

93 hole), which prevents electron-hole recombination and subsequent carrier loss for a higher  
94 conversion efficiency in photocatalysis. Charge separation can be calculated as the weighted  
95 average of the spatial overlap ( $\Lambda$ ) between virtual and occupied Kohn-Sham orbitals in the  
96 lowest excited singlet state, which can be obtained from time-dependent DFT (TDDFT)  
97 calculations.<sup>21</sup> Aiming for cost-effectiveness, here we adopt a previously reported strategy  
98 that allows for using ground-state unrestricted Kohn-Sham (UKS) DFT calculations (PBE  
99 based and PBE0 adjusted, see Figure S1) for charged doublets, *i.e.* -1 for electron injection  
100 and +1 for hole injection.<sup>21</sup> In this case, the charge separation descriptor can be estimated  
101 similarly, but now considering the averaged spatial overlap between the highest occupied  
102 (HOMO( $\alpha$ )) and lowest unoccupied (LUMO( $\beta$ )) molecular orbitals of the electron and the  
103 hole injection, respectively. When the photo-generated charges are spatially separated, this  
104 could favor long lifetimes and low recombination rates. Here we also refer to the overlap  
105 as the “charge recombination descriptor” to intuitively point out lower overlaps as optimal  
106 values for lower charge recombination and more separated charges.

107 **Charge-carrier mobility descriptor** Lastly, to qualitatively evaluate charge-carrier  
108 mobility, the carrier effective masses ( $m^*$ ) were computed. According to the Bardeen-  
109 Shockley model,<sup>21-23</sup>  $m^*$  is inversely proportional to the electronic charge-carrier mobility.  
110 Therefore lower values of  $m^*$  are associated with higher carrier mobility. This strategy avoids  
111 the computation of the bulk modulus and the Bardeen-Shockley deformation potential for the  
112 band edges, which would be necessary for computing charge-carrier mobility requiring excessive  
113 computational resources for screening the entire database. In the parabolic approximation,  
114 the effective mass tensor can be reduced to a scalar quantity and can be computed directly  
115 from the band structure, taking into account the curvature of the VB (for  $m^*$  of holes) and  
116 CB (for  $m^*$  of electrons).<sup>22</sup>

117 **PBE vs PBE0** A challenge with extended structures such as metal-organic frameworks  
118 (MOFs) and COFs is that their unit cell contains many atoms, which makes simulations at

119 high fidelity computationally prohibitive. One way to approach the cost *vs* accuracy issue,  
120 as previously reported for MOFs, is to employ a scheme to evaluate the DFT descriptors  
121 at a GGA-level (e.g., PBE<sup>24</sup>), but making use of a post-processing empirical adjustment to  
122 reproduce hybrid functional (e.g., PBE0) results.<sup>15,21</sup> The hypothesis that such an adjustment  
123 exists is based on the systematic employment of 25% of Hartree-Fock (HF) exact exchange  
124 in PBE0.<sup>25,26</sup> Moreover, the nature of the orbitals contributing to the band gap in COFs  
125 is mostly unchanged between PBE and PBE0. Unlike MOFs, most COFs do not contain  
126 transition and post-transition metals. Their organic element composition reduces the presence  
127 of the charge transfer mechanism in MOFs like ligand-to-metal and metal-to-ligand charge  
128 transfer, which would require higher levels of theory than hybrid functionals.

129 To apply this scheme to the database, we first tested the correlation between PBE and  
130 PBE0 descriptors values for a small subset. We manually selected 20 COFs to compose a  
131 representative subset where we could evaluate the above-mentioned PBE-based strategy to  
132 determine the validity of the strategy in our systems of interest. The dataset is chosen to  
133 contain 2D as well as 3D COFs, also including structures with heteroatoms, and is displayed  
134 in Table S1. Figure 1 shows that PBE and PBE0 display a linear relationship for ionization  
135 potential (IP), electron affinity (EA), and band gap energies ( $R^2$  rounded values of 0.99,  
136 1.00, and 0.99, respectively), even more than MOFs ( $R^2$  values of 0.92, 0.98, and 0.93  
137 respectively).<sup>15</sup> For band gap values, we observed the well-established band gap opening  
138 effect of hybrids compared to GGA functionals.<sup>12</sup> Similarly, the charge separation descriptor  
139 can be empirically adjusted to PBE0 values based on the correlation displayed in Figure S1.<sup>21</sup>

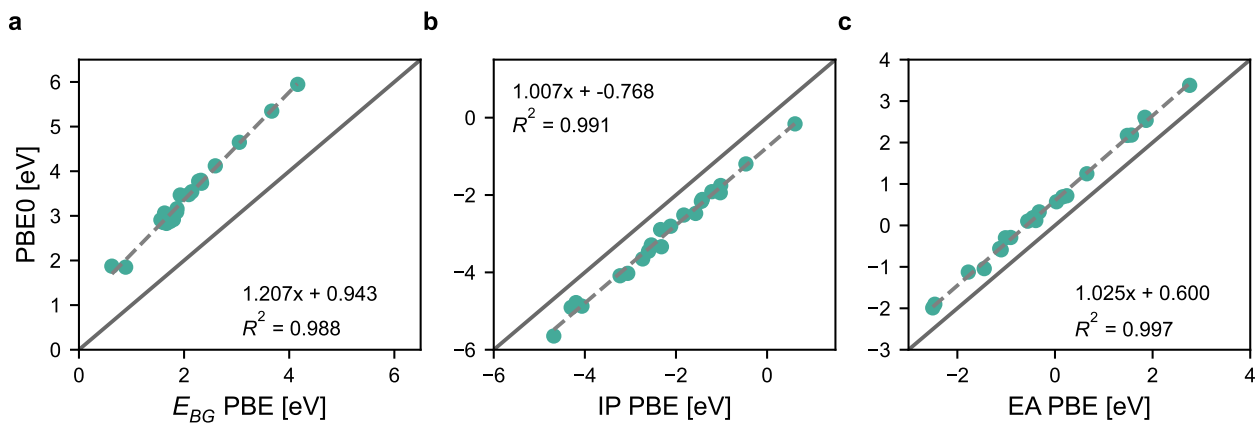


Figure 1: PBE and PBE0 correlation for ionization potential (IP), electron affinity (EA) and band gap values in a set of 20 selected CURATED COFs (see Table S1).

140 Figure 2 depicts the workflow we developed to compute the photocatalytic descriptors,  
 141 with empirical adjustments performed during data treatment. More details regarding the  
 142 decision-making process for the parameters in the workflow are displayed in the SI.

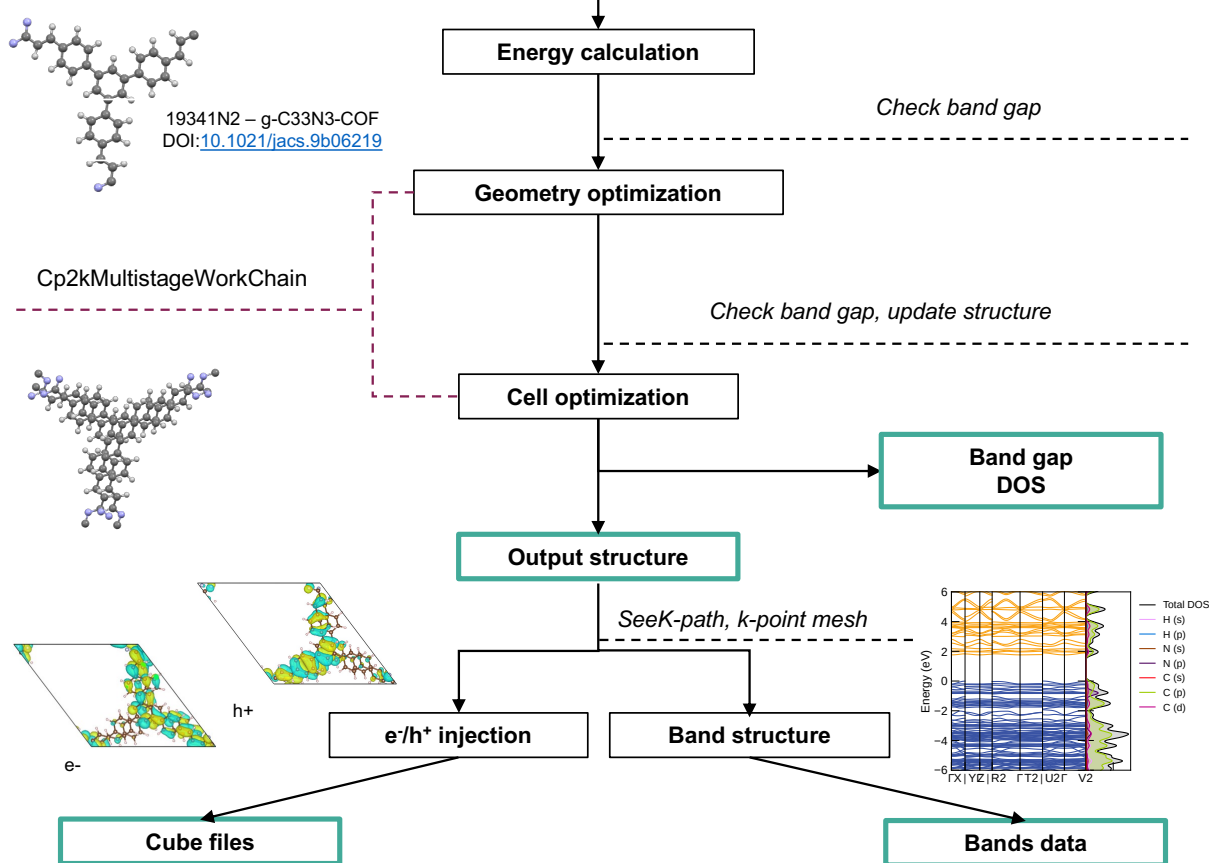


Figure 2: Flowchart of the workflow developed for this screening study. It takes as input the structures from the CURATED COFs database (box highlighted in Persian indigo), then checks the number of atoms and lattice parameters. The next step is a single-point energy calculation. If this calculation confirms that we have a closed-shell system with a semiconducting band, the structure is optimized. From the optimized structure, the workflow computes the main outputs (boxes highlighted in jungle green) utilized to calculate our photocatalytic DFT descriptors, namely, band gap and band alignment (with band gap and cube files printed after optimization), charge separation (with cube files from electron and hole injection) and charge carrier effective masses (with bands data).

## 143 Results and discussion

144 From now on, the case study of overall water splitting (OWS) is considered. The sunlight-  
 145 driven overall splitting of water in H<sub>2</sub> and O<sub>2</sub> is often referred to as the "Holy Grail" in the  
 146 energy landscape, as it is a renewable way of generating energy carriers in a simple but robust



147 strategy from clean and widely available energy sources.<sup>27,28</sup> Although OWS for COFs does  
148 not come without challenges, e.g., slow kinetics of OER and insufficient driving force from  
149 photogenerated charge carriers,<sup>29,30</sup> this case study can guide the discussion, especially for  
150 the preliminary evaluation of thermodynamic feasibility. This can be evaluated by band edge  
151 alignment with the redox potentials of the reaction. An analogous analysis could be applied  
152 to any pair of redox reactions, also with sacrificial agents, co-catalysts, and in a Z-scheme.<sup>31</sup>

## 153 **Photocatalytic DFT descriptors**

154 Firstly, we take a closer look at each photocatalytic DFT descriptor. To aid the evaluation of  
155 structure-property relationships for our descriptors, we determined a set of 26 substructures  
156 (see SI for the complete list) based on chemical intuition and on their occurrence as building  
157 blocks (linkages and linkers) and functional groups in COFs.<sup>8,30,32</sup> Searching for the presence  
158 of those substructures in the CURATED COFs allows for methodical pattern-seeking when  
159 it comes to the structure-property relationships. Such a pattern has been shown previously,  
160 indicating benzene-based functional groups with  $C_{3v}$  symmetry and nitrogen-based functional  
161 groups as potential catalytic active sites for OER and HER, respectively.<sup>30</sup> Among the defined  
162 substructures, we proceed to discuss the ones that presented statistically significant effects  
163 on our photocatalytic DFT descriptors, not considering the ones with only a few data points  
164 or that showed no effect.

165 **Energy-based descriptors** 75% of the evaluated CURATED COFs have their band gaps  
166 in the range of visible light ( $1.6 \text{ eV} < E_{\text{bg}} < 3.2 \text{ eV}$ ). Structural analysis shows that most  
167 structures containing porphyrin, pyrene, triphenylamine, and 2,4,6-triphenyl-1,3,5-triazine  
168 (TPTA, with triazine linkage) have their PBE0-adjusted band gaps within the visible range  
169 (Figure 3). This observation agrees with the photophysical nature of these organic groups  
170 known for having visible-light absorbing properties.<sup>13,23,33-38</sup> The presence of these groups  
171 has been reported for applications involving visible light absorption in COFs.<sup>33,39-41</sup>

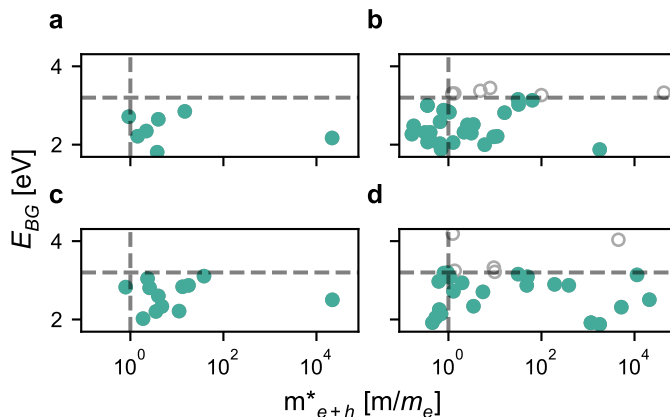


Figure 3: All COFs containing a) porphyrin, b) pyrene, c) triphenylamine, and d) 2,4,6-triphenyl-1,3,5-triazine. Jungle green dots represent structures among them with band gaps in the visible range (porphyrin and triphenylamine 100%, pyrene 83%, 2,4,6-triphenyl-1,3,5-triazine 85%). Grey circles represent structures with those functional groups but out of the visible range (porphyrin and triphenylamine 0%, pyrene 17%, and 2,4,6-triphenyl-1,3,5-triazine 15%). The horizontal line represents the upper limit of the visible light range, the vertical line represents  $m_{e+h}^* = 1m_e$ .

172 Moreover, 14% of the COFs' ionization potential (IP) and electron affinity (EA) values  
 173 straddle the OER and HER potentials, all with band gaps within the visible range. Figure 4  
 174 shows the band edge alignment for the filtered structures in this case study. Indeed, we see  
 175 in Figure 4 that all values for electron affinity are above the hydrogen evolution reaction  
 176 potential (jungle green dashed line), and all values for ionization potential are below the  
 177 oxygen evolution reaction potential (Persian indigo dashed line). Such straddling indicates  
 178 thermodynamic feasibility for OWS with visible light absorption (the black dashed line is the  
 179 maximum value in the visible range). Tighter alignment, *i.e.* lower band gaps ( $E_{bg} < 2.36$  eV)  
 180 in this plot are desired to achieve the minimum requirement of 10% solar-to-hydrogen (STH)  
 181 efficiency for profitable industrialization.<sup>42</sup> Furthermore, the filtered structures can also be  
 182 investigated as photocatalysts for individual HER and OER.

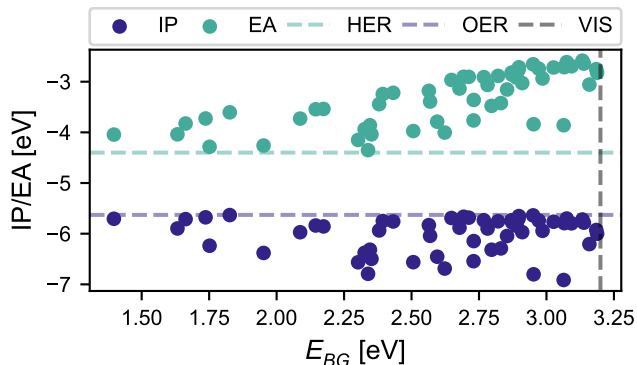


Figure 4: Simultaneous filtering of the energy-based DFT descriptors computed for 419 CURATED COFs. For the case study of overall water splitting, good candidates should have their IP and EA straddling the redox potentials of HER (jungle green dashed line) and OER (Persian indigo dashed line), all aligned to vacuum, and band gap in the visible range (grey dashed line as the maximum value). IP and EA in the same vertical line correspond to the same structure.

183 We highlight that all calculations are kept at the GGA level, with the PBE functional,  
 184 and posteriorly adjusted empirically to PBE0 values. This choice is justified by our screening  
 185 approach, considering the large number of COFs. However, DFT, even with hybrid functionals,  
 186 can present shortcomings regarding the prediction of fundamental band gaps and IP/EA levels.  
 187 For GGA functionals, one example is the difficulty in capturing excitonic effects in organic  
 188 systems, which can be in the order of a few eV and severely impact visible light absorption.<sup>18</sup>  
 189 Therefore, this approach might not be enough when compared to more accurate calculations,  
 190 but it can at least describe the nature of the electronic properties of COFs. Moreover, the  
 191 strategy adopted here allows for a cost-effective way of shortlisting photocatalyst candidates,  
 192 which can later be redirected for more accurate calculations.

193 **Charge separation descriptor** The charge separation descriptors computed in this  
 194 work range between 0.037 and 0.931 (it can go from 0 to 1). To test the validity of our  
 195 charge separation descriptor, we compared our results with reported lifetimes in COFs. Our  
 196 computed values agree qualitatively with experimental results of charge carrier lifetime for,  
 197 e.g., COF-366 (low  $\Lambda=0.3$ , lifetime of  $\approx 80 \mu\text{s}$ ) and  $\text{N}_3\text{-COF}$  (high  $\Lambda=0.7$ , average lifetime of

198  $\approx 4$  ns).<sup>43,44</sup> Considering that lower values of  $\Lambda$  are an indication of lower chances of electron-  
199 hole recombination, we filtered the structures presenting  $\Lambda$  less than 0.5 as potentially  
200 favorable for charge separation. The structures obtained after this filter represent 28% of the  
201 database. With a lower threshold of 0.15, 13 structures are filtered, 4 of them composing a  
202 series of multiple-component donor-acceptor COFs (MC-COF-TPs), strategically designed to  
203 contain spatially separated electron donor and acceptor groups.<sup>45</sup> Those COFs contain the  
204 group 2,3,6,7,10,11-hexahydroxytriphenylene (TP) as knots, benzene-1,4-dialdehyde, nitro-*p*-  
205 phenylenediamine and *p*-phenylenediamine as electron donors and 2,1,3-benzothiadiazole-4,7-  
206 diboronic acid (BTDADA) as an electron acceptor, with N, B, and S heteroatoms present and  
207 spatially separated in each structure.<sup>45</sup> The authors state that charge transfer is triggered  
208 from TP to BTDADA and that the sequenced  $\pi$ -arrays may play an important role in the  
209 electronic correlations.<sup>45</sup> The presence of groups that can stabilize charge carriers is crucial  
210 for enhancing photocatalytic activity and is desired if one would like to design COFs with low  
211 detrimental charge recombination.<sup>46</sup> The remaining nine structures with the lowest computed  
212 charge recombination descriptors ( $\Lambda < 0.15$ ) are BP-COF-1 and BP-COF-2 (both with B, S, P,  
213 O, and F as heteroatoms), PIA-AA and PIC-AA (both with dicarboximide groups), CCOF-1,  
214 NN-TAPH-COF, (R)-DTP-COF, DhaTab, and COF-119.<sup>47-52</sup> Among them, triphenylbenzene  
215 seems to be a common group (for DhaTab, PIC-AA, and (R)-DTP-COF).

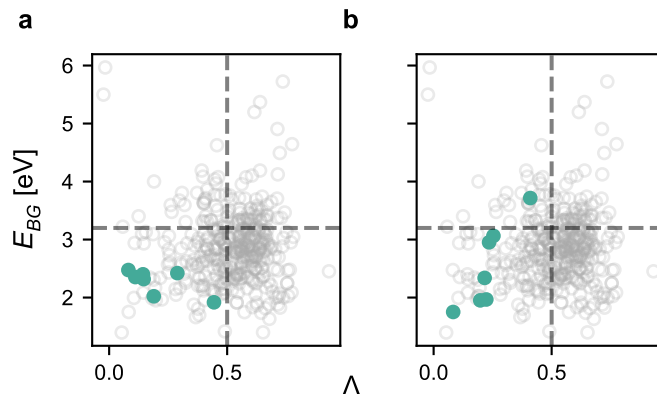


Figure 5: Structural analysis of all COFs distributed by their band gap and overlap values, with jungle green dots representing all structures that contain a) thiadiazole, or b) phthalimide. The horizontal line represents the upper limit of the visible light range, and the vertical line represents  $\Lambda = 0.5$ .

216 Moreover, our substructure-based structural analysis shows that the presence of thiadiazole  
 217 and phthalimide is associated with low overlap values, as displayed in Figure 5. All COFs  
 218 with those substructures have a charge separation descriptor lower than 0.5. Statistical  
 219 analysis with bootstrapped effect sizes corroborates the lowering of charge recombination  
 220 descriptor with the presence of those groups (see Figures S14 and S15).

221 **Charge-carrier mobility descriptor** Concerning the charge-carrier mobility descriptor,  
 222 67% of the COFs have effective masses of both electron and hole below ten times the electron  
 223 rest mass ( $m_e$ ). The threshold is chosen because most of the effective masses reported for  
 224 COFs with high conductivity in the literature are below this value.<sup>44,53–55</sup> At a much tighter  
 225 threshold of 1  $m_e$ , still, 35% remain, among which only 6% are 3D COFs. Figure 6 shows a  
 226 distribution of the effective masses of both electron and hole for the evaluated CURATED  
 227 COFs. Out of the structures with effective masses of either electron or hole higher than 100  
 228  $m_e$ , 18% are 3D COFs.

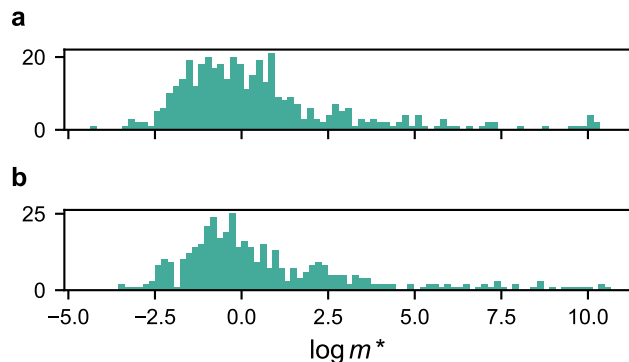


Figure 6: Distribution of effective masses of a) electron and b) hole computed for 419 CURATED COFs.

229 When comparing the COFs with very low ( $m^* < 1 m_e$ ) and very high ( $m^* > 100 m_e$ ) effective  
 230 masses, it was observed that COFs with low effective masses uniquely contain  $\beta$ -ketoenamine  
 231 linkages with the group 2,4,6-trimethanimidoylbenzene-1,3,5-triol (TIBT), and COFs with  
 232 high effective masses uniquely contain glutarimide (with dicarboximide group). In Figure 7,  
 233 a pattern can be seen for  $\beta$ -ketoenamine-linked COFs with TIBT, its presence occurring  
 234 mostly on COFs with low effective masses and appropriate IP/EA values for aligning with  
 235 HER. Statistical analysis with bootstrapped effect sizes shows a significant difference between  
 236 the means of effective masses of COFs with and without  $\beta$ -ketoenamine linkage with TIBT  
 237 (lowering of 2 units in the log scale for both electron and hole Figures S12,S13). Indeed,  
 238  $\beta$ -ketoenamine-linked COFs usually display good photocatalytic properties for HER, with  
 239 increased stability with respect to their imine counterparts.<sup>8,56</sup> However, the same COFs,  
 240 except for a few, present higher values of the computed charge recombination descriptor  
 241 (Figure 7b). It has been suggested that introducing donor-acceptor units to COFs with  
 242 this linkage can enhance their photocatalytic activity by stabilizing excited charge transfer  
 243 processes.<sup>56</sup>

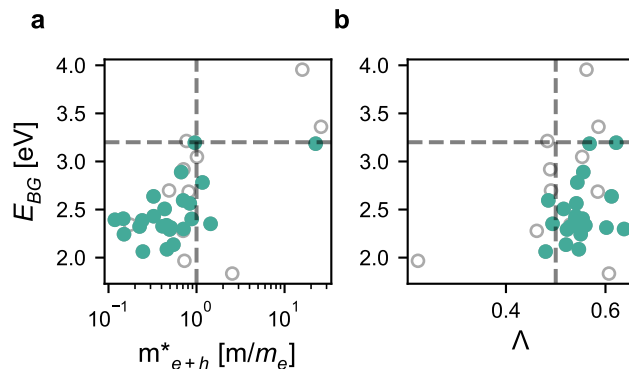


Figure 7: Structural analysis of all the  $\beta$ -ketoenamine-linked COFs with TIBT. Jungle green dots represent structures with band edges aligning with the HER redox potential, and grey circles represent those that do not align. HER alignment occurs mostly in structures with low effective masses and appropriate band gaps but relatively high overlap. The horizontal line represents the upper limit of the visible light range, and the vertical line represents in a)  $m_{e+h}^* = 1m_e$ , and in b)  $\Lambda = 0.5$ .

244 Concerning the before-mentioned MC-COF-TPs series with low charge recombination  
 245 descriptors, their uniformly distributed N and S heteroatoms are also expected to enhance  
 246 charge-carrier mobility.<sup>57</sup> Such observation is corroborated by the computed  $m^*$  for both  
 247 electron and hole for MC-COF-TPs, that range between 5e–10 to 13  $m_e$ , with the exception  
 248 of  $m_h^*$  for MC-COF-TP-E<sub>1</sub><sup>2</sup>E<sub>2</sub><sup>1</sup>. In summary, when designing COFs to enhance charge-  
 249 carrier mobility, choosing 2D dimensionality and  $\beta$ -ketoenamine linkage with TIBT could be  
 250 advantageous.

251 Moreover, the presence of dicarboximide functional groups was associated with lower charge  
 252 recombination descriptors, but higher effective masses. A similar pattern is present for CCOF-  
 253 1, with high effective masses but low charge recombination descriptor. Such observations  
 254 could derive from lower band dispersion, which reduces the possibility of detrimental charge  
 255 recombination, but can also reduce charge-carrier mobility. In fact, this behavior is observed  
 256 in CCOF-1, with calculated band dispersion for VB and CB of 0.72 and 1.4 meV, respectively.  
 257 Those values represent the absolute difference between the highest and lowest energy values  
 258 for each band.

## 259 Shortlisted candidates for the case study of OWS

260 Combining the optimal values for all the descriptors, we end up with a set of 13 COFs that  
261 are promising for the case study of overall water splitting. The structures of interest are  
262 represented by the dark green and blue dots in the specified bottom-left region in Figure 8a,  
263 and detailed in Table S2. A thorough literature review shows that, to date, some of the filtered  
264 COFs have been explored for different photocatalytic processes, such as CO<sub>2</sub> reduction,<sup>58</sup>  
265 which corroborates their usage as light harvesters.

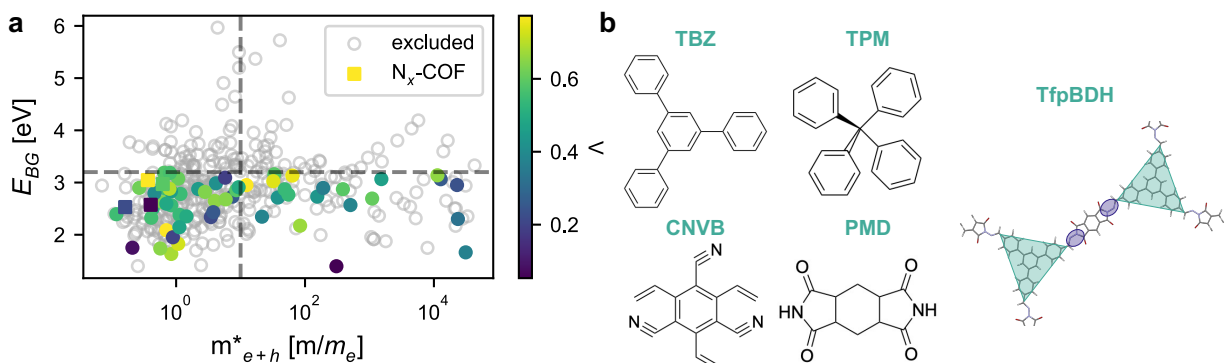


Figure 8: a) Simultaneous filtering of all the computed DFT descriptors for 419 CURATED COFs for the case study of overall water splitting. The region of interest is in the lower left region, which indicates more appropriate band gaps and low carrier effective masses. Grey dots are structures whose band edges do not straddle HER and OER redox potentials. Dark colors indicate a lower possibility of charge recombination. N<sub>x</sub>-COFs filtered for HER and already investigated for this application are represented by colored squares. b) Common substructures in the set of 13 filtered COFs for OWS. To the right, the backbone is highlighted, which is similar to the donor-acceptor COFs designed for OWS, with HER and OER active sites highlighted in jungle green and Persian indigo, respectively.<sup>30</sup>

266 Most filtered COFs, however, have not yet been explored for photocatalytic HER/OER  
267 (79%, see Table S2), thus highlighting the usefulness of the current work and suggesting further  
268 theoretical and/or experimental investigation. Among the 13 COFs, common substructures are  
269 1,3,5-(triphenyl)benzene, pyrometallic diimide, tetraphenylmethane, and 1,3,5-tricyano-2,4,6-  
270 tris(vinyl)benzene, see Figure 8b. Common linkages are imine, imide, azo, and  $\beta$ -ketoenamine  
271 (with TIBT). Moreover, some COFs in the final list, such as TfpBDH and PI-COF-SR,  
272 display a similar backbone compared to donor-acceptor COFs designed strategically for



273 photocatalytic OWS (Figure 8b).<sup>30</sup>

274 As a proof of concept, N<sub>x</sub>-COFs (x=0-3) were evaluated by this work as prospective  
275 candidates for photocatalytic HER and are already reported for this application.<sup>59</sup> Indeed,  
276 it showed proper alignment of IP/EA, band gap values within the visible range that agree  
277 reasonably with experimental results and good results for effective masses (below 5 m<sub>e</sub>), see  
278 Table S3 for more details. Figure 8a represents this series in colored squares. N<sub>3</sub>-COF, in  
279 particular, has its IP/EA straddling both HER and OER, thus could also be a candidate for  
280 OWS. Although its charge separation descriptor is slightly higher than our threshold of 0.5, it  
281 was nevertheless reported among the N<sub>x</sub>-COF series as the most effective HER photocatalyst  
282 when triethanolamine is chosen as the sacrificial donor.

## 283 **Structure-property relationship**

284 Figure 9 summarizes the effect of the defined building blocks and functional groups whose  
285 presence statistically affects at least one of our photocatalytic DFT descriptors. The presence  
286 of  $\beta$ -ketoenamine with TIBT, for example, promotes a statistically significant lowering of  
287 charge carrier effective masses, but increases the values of the charge recombination descriptor.  
288 More details on the statistical analysis are displayed in the SI, showing as an example the  
289 statistically-based effect of  $\beta$ -ketoenamine (with TIBT) on each descriptor (Figures S10-S13).

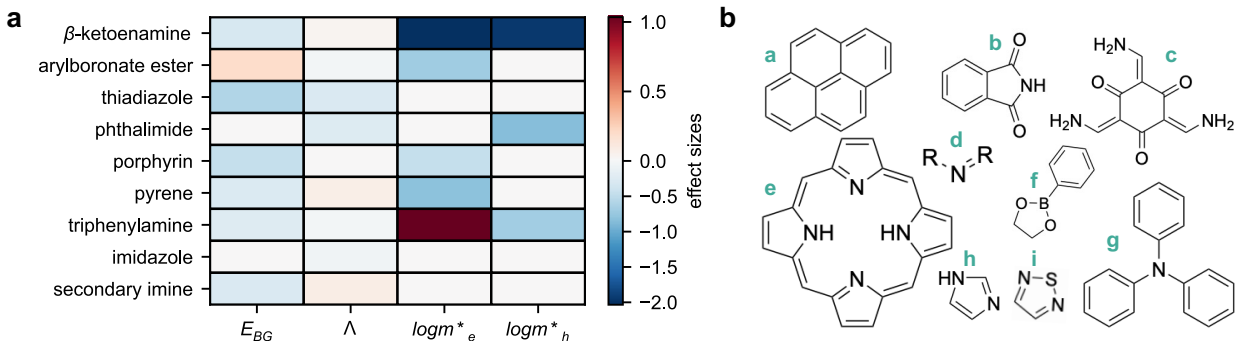


Figure 9: a) Effect of the presence of defined substructures on the band gap, charge recombination descriptor, and effective masses based on statistical analysis with bootstrapped effect sizes. A lowering trend is desired for  $\Lambda$  and  $m^*$ , indicating lower chances of electron and hole recombination, and higher charge carrier mobility. b) Visualization of substructures, namely, a. pyrene, b. phthalimide, c. TIBT ( $\beta$ -ketoenamine linkage), d. secondary imine, e. porphyrin, f. arylboronate ester (2-phenyl-1,3,2-dioxaborolane), g. triphenylamine, h. imidazole, and i. 1,2,5-thiadiazole.

290 Furthermore, topology analysis with CrystalNets.jl<sup>60</sup> in the “all nodes” clustering was  
 291 successfully performed for 300 structures. The distribution of topologies found is displayed in  
 292 Figure S16. The results show that most structures aligned for OWS and individual HER  
 293 and OER present honeycomb (**hcb**), augmented honeycomb (**hca**), **fes**, and **hnb** topologies.  
 294 For the case of HER, although the occurrence of **hbn** topology is practically unchanged in  
 295 the filtered COFs (2.3% of occurrence in all COFs, 2.7% in the filtered ones for HER), we  
 296 noticed an increase in the occurrence of **hca** (64.5% of occurrence in all COFs, 75.7% in the  
 297 filtered ones for HER), **hcb** (6.4% of occurrence in all COFs, 10.8% in the filtered ones for  
 298 HER), and **fes** (5.0% of occurrence in all COFs, 10.8% in the filtered ones for HER). In the  
 299 literature, COFs that have been reported for HER oftentimes display honeycomb (**hcb** and  
 300 **hca**) topologies.<sup>61,62</sup> Our findings suggest that **fes** nets could be another possible direction of  
 301 exploration for photocatalytically active COFs.

## Other photo-redox reactions

To allow for an in-depth analysis of the evaluated COFs, we have chosen the study case of overall water splitting. However, as previously mentioned, the strategy adopted here can be applied to any pair of redox reactions without the need to perform further calculations. As a demonstration of the versatility of this work, we developed a bokeh application that allows for interactive filtering of the evaluated COFs. Such filtering can be done by choosing different redox reactions and different thresholds for the charge carrier mobility and charge recombination descriptors. The video in the supplementary materials exemplifies the usage of this application by filtering candidates for photocatalytic CO<sub>2</sub> reduction to methanol, with triethanolamine (TEOA) as a sacrificial agent. The process of reducing CO<sub>2</sub> to value-added chemicals such as methanol is a compelling alternative to recycle CO<sub>2</sub> from the environment.<sup>63</sup> After applying the desired filters, which can also be customized to feasible values, it is possible to obtain the dataset of the filtered COFs.

## Conclusions

The screening approach employed by this work allowed the shortlisting of photocatalytically active COFs based on a cost-effective calculation of DFT-based descriptors. We selected 13 COFs as prospective photocatalysts for OWS after screening the database for alignment to redox potentials, visible light absorption, charge separation, and charge-carrier mobility descriptors. The list of selected COFs for HER contains the series of N<sub>x</sub>-COF (x=0-3) already studied experimentally for this purpose. Interestingly, our approach can seamlessly be extended to filter candidates for any desired pair of photo-redox reactions.

Structural analysis for each DFT descriptor provided suggestions for the rational design of photocatalytically active COFs. Porphyrin, pyrene, triphenylamine, and TPTA-containing COFs were associated with visible light absorption, which can be considered when designing photocatalytic COFs to harvest sunlight. Most  $\beta$ -ketoenamine-linked COFs with TIBT in

327 the database have their IPs/EAs aligned to the HER potential. Concerning charge separation,  
328 COFs containing thiadiazole and phthalimide groups display a statistically significant lowering  
329 of the computed averaged spatial overlap that assesses the likelihood of charge recombination.  
330 Furthermore, the choice of 2D dimensionality and  $\beta$ -ketoenamine linkages with TIBT can  
331 benefit the design of COFs with enhanced charge-carrier mobility.

332 We highlight that other aspects need to be further considered for evaluating photocatalytic  
333 performance, such as photo-stability, stacking modes, and kinetics, which are open questions  
334 for this screening approach. Suggested next steps are the experimental evaluation of the  
335 shortlisted COFs in Table S2 for OWS and further theoretical investigations with higher  
336 accuracy. Future works could also address the influence of how stacking modes and statistical  
337 stacking order can affect our photocatalytic descriptors. Altogether, this work can pave the  
338 way for using in-silico methodologies to design COFs for photocatalysis.

## 339 Computational methods

340 The Automated Interactive Infrastructure and Database for Computational Science (Ai-  
341 iDA,<sup>64,65</sup> v1.6.5) was used as a workflow manager to perform the DFT calculations for 419  
342 structures from the CURATED COFs database.<sup>11</sup> A new workchain was built as depicted  
343 by the flowchart in Figure 2 based on workchains for multistage optimization and base  
344 calculations from the plugins aiida-cp2k and aiida-lsmo. The logic of the developed workchain  
345 consists of evaluating the band gap to ensure a closed-shell system/semiconducting band gap,  
346 followed by optimization of the cell parameters and calculations of our DFT descriptors for  
347 photocatalysis.<sup>15,21</sup>

348 Ground-state unrestricted Kohn-Sham (UKS) DFT calculations were employed for electron  
349 and hole injection to evaluate the charge separation descriptor as previously defined.<sup>21</sup>

350 Electronic chemical potentials were aligned to vacuum as reported by Fumanal et al.<sup>15</sup>,  
351 based on the procedure established by Butler et al.<sup>16</sup> The band extrema energies were

352 corrected with our empirical adjustment to mimic PBE0 values.

353 For the charge separation descriptor, an in-house code was developed to compute the  
354 averaged spatial overlap of the cube files for electron and hole injection.<sup>66</sup>

355 The parabolic approximation implemented in sumo library<sup>67</sup> was used to compute effective  
356 masses of electrons and holes based on the electronic bands' dispersion in the reciprocal  
357 space.<sup>21,22</sup>

358 More details about the DFT calculations can be found in the Supporting Informa-  
359 tion. Structural analysis was performed with the CSD substructure search Python API via  
360 SMARTS,<sup>68,69</sup> and we used CrystalNets.jl<sup>60</sup> for topology analysis. It was necessary to consider  
361 flexible SMARTS definition, *i.e.* not explicitly specifying aromaticity or unsaturations, for  
362 proper recognition with the CSD substructure search due to incompatibilities in bond lengths.  
363 Other computational tools utilized in this work are detailed in the Supporting Information.

## 364 **Statistics**

365 We performed statistical analysis to determine whether the presence of a building block  
366 or functional group could have positive, negative, or no effects on our photocatalytic DFT  
367 descriptors. We employed bootstrapped effect sizes with the DABEST package<sup>70</sup> for quantita-  
368 tive estimation of effect sizes. Detailed information on the statistical tests is available as a  
369 supplementary material.

## 370 **Acknowledgement**

371 The authors acknowledge PRACE and MARVEL for awarding access to Piz Daint (project ID:  
372 pr128) and Eiger (project ID: mr30) at the Swiss National Supercomputing Centre (CSCS),  
373 Switzerland. This project has received funding from the European Union's Horizon 2020  
374 research and innovation programme under the Marie Skłodowska-Curie grant agreement No.  
375 945363.

## 376 **Supporting Information Available**

377 Further details on the datasets, computational methods, statistical analysis and preliminary  
378 tests are detailed in the Supporting Information.

## 379 **Authors contributions**

380 A.O.-G., K.M.J. and B.M. designed the research strategy, K.M.J. and B.M. developed the  
381 workflow, B.M. performed data analysis. B.M. wrote the first draft. B.M., A.O.-G., K.M.J.  
382 and B.S. contributed to writing and revising the manuscript, directing the work and providing  
383 crucial inputs.

## 384 **Data availability**

385 The aiida workflow and post-processing codes utilized by this work are available on [https://github.com/bmourino/cof\\_photocatalysis](https://github.com/bmourino/cof_photocatalysis). The final dataset with the values for all the  
386 descriptors, and a separate dataset containing details on statistical analysis with bootstrapped  
387 effect sizes are available on <https://doi.org/10.5281/zenodo.7590815>. The interactive  
388 application developed is available on <https://go.epfl.ch/cof-photocatalysis-app>.

## 390 **Ethics declarations**

## 391 **Competing interests**

392 The authors declare no competing interests.

## References

- (1) Galushchinskiy, A.; González-Gómez, R.; McCarthy, K.; Farràs, P.; Savateev, A. Progress in Development of Photocatalytic Processes for Synthesis of Fuels and Organic Compounds under Outdoor Solar Light. *Energy & Fuels* **2022**, *36*, 4625–4639.
- (2) Melchionna, M.; Fornasiero, P. Updates on the Roadmap for Photocatalysis. *ACS Catalysis* **2020**, *10*, 5493–5501.
- (3) Cote, A. P.; Benin, A. I.; Ockwig, N. W.; O’Keeffe, M.; Matzger, A. J.; Yaghi, O. M. Porous, Crystalline, Covalent Organic Frameworks. *Science* **2005**, *310*, 1166–1170.
- (4) Diercks, C. S.; Yaghi, O. M. The atom, the molecule, and the covalent organic framework. *Science* **2017**, *355*.
- (5) Zhang, Y.; Položij, M.; Heine, T. Statistical Representation of Stacking Disorder in Layered Covalent Organic Frameworks. *Chemistry of Materials* **2022**, *34*, 2376–2381.
- (6) Chen, R.; Wang, Y.; Ma, Y.; Mal, A.; Gao, X.-Y.; Gao, L.; Qiao, L.; Li, X.-B.; Wu, L.-Z.; Wang, C. Rational design of isostructural 2D porphyrin-based covalent organic frameworks for tunable photocatalytic hydrogen evolution. *Nature Communications* **2021**, *12*.
- (7) Nguyen, H. L.; Alzamy, A. Covalent Organic Frameworks as Emerging Platforms for CO<sub>2</sub> Photoreduction. *ACS Catalysis* **2021**, *11*, 9809–9824.
- (8) Li, Y.; Song, X.; Zhang, G.; Wang, L.; Liu, Y.; Chen, W.; Chen, L. 2D Covalent Organic Frameworks Toward Efficient Photocatalytic Hydrogen Evolution. *ChemSusChem* **2022**, *15*, e202200901.
- (9) Ongari, D.; Talirz, L.; Smit, B. Too Many Materials and Too Many Applications: An Experimental Problem Waiting for a Computational Solution. *ACS Central Science* **2020**, *6*, 1890–1900.

- 417 (10) Kanal, I. Y.; Owens, S. G.; Bechtel, J. S.; Hutchison, G. R. Efficient Computational  
418 Screening of Organic Polymer Photovoltaics. *The Journal of Physical Chemistry Letters*  
419 **2013**, *4*, 1613–1623.
- 420 (11) Ongari, D.; Yakutovich, A. V.; Talirz, L.; Smit, B. Building a Consistent and Repro-  
421 ducible Database for Adsorption Evaluation in Covalent–Organic Frameworks. *ACS*  
422 *Central Science* **2019**, *5*, 1663–1675.
- 423 (12) Kronik, L.; Stein, T.; Refaely-Abramson, S.; Baer, R. Excitation Gaps of Finite-  
424 Sized Systems from Optimally Tuned Range-Separated Hybrid Functionals. *Journal of*  
425 *Chemical Theory and Computation* **2012**, *8*, 1515–1531, PMID: 26593646.
- 426 (13) Ortega-Guerrero, A.; Fumanal, M.; Capano, G.; Smit, B. From Isolated Porphyrin  
427 Ligands to Periodic Al-PMOF: A Comparative Study of the Optical Properties Using  
428 DFT/TDDFT. *The Journal of Physical Chemistry C* **2020**, *124*, 21751–21760.
- 429 (14) Hait, D.; Head-Gordon, M. Delocalization Errors in Density Functional Theory Are  
430 Essentially Quadratic in Fractional Occupation Number. *The Journal of Physical*  
431 *Chemistry Letters* **2018**, *9*, 6280–6288.
- 432 (15) Fumanal, M.; Capano, G.; Barthel, S.; Smit, B.; Tavernelli, I. Energy-based descriptors  
433 for photo-catalytically active metal–organic framework discovery. *J. Mater. Chem. A*  
434 **2020**, *8*, 4473–4482.
- 435 (16) Butler, K. T.; Hendon, C. H.; Walsh, A. Electronic Chemical Potentials of Porous  
436 Metal–Organic Frameworks. *Journal of the American Chemical Society* **2014**, *136*,  
437 2703–2706, PMID: 24447027.
- 438 (17) Tamirat, A. G.; Rick, J.; Dubale, A. A.; Su, W.-N.; Hwang, B.-J. Using hematite  
439 for photoelectrochemical water splitting: a review of current progress and challenges.  
440 *Nanoscale Horizons* **2016**, *1*, 243–267.



- 441 (18) Wang, H.; Jin, S.; Zhang, X.; Xie, Y. Excitonic Effects in Polymeric Photocatalysts.  
442 *Angewandte Chemie International Edition* **2020**, *59*, 22828–22839.
- 443 (19) Botti, S.; Sottile, F.; Vast, N.; Olevano, V.; Reining, L.; Weissker, H.-C.; Rubio, A.;  
444 Onida, G.; Sole, R. D.; Godby, R. W. Long-range contribution to the exchange-correlation  
445 kernel of time-dependent density functional theory. *Physical Review B* **2004**, *69*.
- 446 (20) Janesko, B. G.; Henderson, T. M.; Scuseria, G. E. Screened hybrid density functionals  
447 for solid-state chemistry and physics. *Phys. Chem. Chem. Phys.* **2009**, *11*, 443–454.
- 448 (21) Fumanal, M.; Ortega-Guerrero, A.; Jablonka, K. M.; Smit, B.; Tavernelli, I. Charge  
449 Separation and Charge Carrier Mobility in Photocatalytic Metal-Organic Frameworks.  
450 *Advanced Functional Materials* **2020**, *30*, 2003792.
- 451 (22) Muschiello, C.; Oberhofer, H. Aspects of semiconductivity in soft, porous metal-organic  
452 framework crystals. *The Journal of Chemical Physics* **2019**, *151*, 015102.
- 453 (23) Kinik, F. P.; Ortega-Guerrero, A.; Ebrahim, F. M.; Ireland, C. P.; Kadioglu, O.; Mace, A.;  
454 Asgari, M.; Smit, B. Toward Optimal Photocatalytic Hydrogen Generation from Water  
455 Using Pyrene-Based Metal–Organic Frameworks. *ACS Applied Materials & Interfaces*  
456 **2021**, *13*, 57118–57131, PMID: 34817166.
- 457 (24) Perdew, J. P.; Burke, K.; Ernzerhof, M. Generalized Gradient Approximation Made  
458 Simple. *Phys. Rev. Lett.* **1996**, *77*, 3865–3868.
- 459 (25) Baerends, E. J. From the Kohn–Sham band gap to the fundamental gap in solids. An  
460 integer electron approach. *Phys. Chem. Chem. Phys.* **2017**, *19*, 15639–15656.
- 461 (26) Bao, J. L.; Gagliardi, L.; Truhlar, D. G. Self-Interaction Error in Density Functional  
462 Theory: An Appraisal. *The Journal of Physical Chemistry Letters* **2018**, *9*, 2353–2358,  
463 PMID: 29624392.

- 464 (27) Zhou, P.; Navid, I. A.; Ma, Y.; Xiao, Y.; Wang, P.; Ye, Z.; Zhou, B.; Sun, K.; Mi, Z.  
465 Solar-to-hydrogen efficiency of more than 9% in photocatalytic water splitting. *Nature*  
466 **2023**, *613*, 66–70.
- 467 (28) Bie, C.; Wang, L.; Yu, J. Challenges for photocatalytic overall water splitting. *Chem*  
468 **2022**, *8*, 1567–1574.
- 469 (29) Christoforidis, K. C.; Fornasiero, P. Photocatalytic Hydrogen Production: A Rift into  
470 the Future Energy Supply. *ChemCatChem* **2017**, *9*, 1523–1544.
- 471 (30) Wan, Y.; Wang, L.; Xu, H.; Wu, X.; Yang, J. A Simple Molecular Design Strategy for  
472 Two-Dimensional Covalent Organic Framework Capable of Visible-Light-Driven Water  
473 Splitting. *Journal of the American Chemical Society* **2020**, *142*, 4508–4516, PMID:  
474 32043354.
- 475 (31) Wang, Y.; Vogel, A.; Sachs, M.; Sprick, R. S.; Wilbraham, L.; Moniz, S. J. A.; Godin, R.;  
476 Zwijnenburg, M. A.; Durrant, J. R.; Cooper, A. I.; Tang, J. Current understanding and  
477 challenges of solar-driven hydrogen generation using polymeric photocatalysts. *Nature*  
478 *Energy* **2019**, *4*, 746–760.
- 479 (32) *Introduction to Reticular Chemistry*; John Wiley & Sons, Ltd, 2019; Chapter 8, pp  
480 197–223.
- 481 (33) Stegbauer, L.; Zech, S.; Savasci, G.; Banerjee, T.; Podjaski, F.; Schwinghammer, K.;  
482 Ochsenfeld, C.; Lotsch, B. V. Tailor-Made Photoconductive Pyrene-Based Covalent  
483 Organic Frameworks for Visible-Light Driven Hydrogen Generation. *Advanced Energy*  
484 *Materials* **2018**, *8*, 1703278.
- 485 (34) Mohammed, O. F.; Dreyer, J.; Magnes, B.-Z.; Pines, E.; Nibbering, E. T. J. Solvent-  
486 Dependent Photoacidity State of Pyranine Monitored by Transient Mid-Infrared Spec-  
487 troscopy. *ChemPhysChem* **2005**, *6*, 625–636.

- 488 (35) Kinik, F. P.; Ortega-Guerrero, A.; Ongari, D.; Ireland, C. P.; Smit, B. Pyrene-based  
489 metal organic frameworks: from synthesis to applications. *Chemical Society Reviews*  
490 **2021**, *50*, 3143–3177.
- 491 (36) Dumur, F. Recent advances on visible light Triphenylamine-based photoinitiators of  
492 polymerization. *European Polymer Journal* **2022**, *166*, 111036.
- 493 (37) Tiwari, A.; Pal, U. Effect of donor-donor- $\pi$ -acceptor architecture of triphenylamine-based  
494 organic sensitizers over TiO<sub>2</sub> photocatalysts for visible-light-driven hydrogen production.  
495 *International Journal of Hydrogen Energy* **2015**, *40*, 9069–9079.
- 496 (38) Zhang, X.; Jin, R. Rational Design of Low-Band Gap Star-Shaped Molecules With  
497 2,4,6-Triphenyl-1,3,5-triazine as Core and Diketopyrrolopyrrole Derivatives as Arms for  
498 Organic Solar Cells Applications. *Frontiers in Chemistry* **2019**, *7*.
- 499 (39) Fateeva, A.; Chater, P. A.; Ireland, C. P.; Tahir, A. A.; Khimyak, Y. Z.; Wiper, P. V.;  
500 Darwent, J. R.; Rosseinsky, M. J. A Water-Stable Porphyrin-Based Metal-Organic  
501 Framework Active for Visible-Light Photocatalysis. *Angewandte Chemie International*  
502 *Edition* **2012**, *51*, 7440–7444.
- 503 (40) Dai, C.; He, T.; Zhong, L.; Liu, X.; Zhen, W.; Xue, C.; Li, S.; Jiang, D.; Liu, B. 2,4,6-  
504 Triphenyl-1,3,5-Triazine Based Covalent Organic Frameworks for Photoelectrochemical  
505 H<sub>2</sub> Evolution. *Advanced Materials Interfaces* **2021**, *8*, 2002191.
- 506 (41) Luo, B.; Chen, Y.; Zhang, Y.; Huo, J. Benzotrithiophene and triphenylamine based  
507 covalent organic frameworks as heterogeneous photocatalysts for benzimidazole synthesis.  
508 *Journal of Catalysis* **2021**, *402*, 52–60.
- 509 (42) Ng, K. H.; Lai, S. Y.; Cheng, C. K.; Cheng, Y. W.; Chong, C. C. Photocatalytic water  
510 splitting for solving energy crisis: Myth, Fact or Busted? *Chemical Engineering Journal*  
511 **2021**, *417*, 128847.

- 512 (43) Wan, S.; Gandara, F.; Asano, A.; Furukawa, H.; Saeki, A.; Dey, S. K.; Liao, L.;  
513 Ambrogio, M. W.; Botros, Y. Y.; Duan, X.; Seki, S.; Stoddart, J. F.; Yaghi, O. M.  
514 Covalent Organic Frameworks with High Charge Carrier Mobility. *Chemistry of Materials*  
515 **2011**, *23*, 4094–4097.
- 516 (44) Ma, S.; Deng, T.; Li, Z.; Zhang, Z.; Jia, J.; Li, Q.; Wu, G.; Xia, H.; Yang, S.-W.;  
517 Liu, X. Photocatalytic Hydrogen Production on a sp<sup>2</sup>-Carbon-Linked Covalent Organic  
518 Framework. *Angewandte Chemie* **2022**, *134*.
- 519 (45) Huang, N.; Zhai, L.; Coupry, D. E.; Addicoat, M. A.; Okushita, K.; Nishimura, K.;  
520 Heine, T.; Jiang, D. Multiple-component covalent organic frameworks. *Nat. Commun.*  
521 **2016**, *7*, 12325.
- 522 (46) Kailasam, K.; Mesch, M. B.; Möhlmann, L.; Baar, M.; Blechert, S.; Schwarze, M.;  
523 Schröder, M.; Schomäcker, R.; Senker, J.; Thomas, A. Donor-Acceptor-Type Heptazine-  
524 Based Polymer Networks for Photocatalytic Hydrogen Evolution. *Energy Technology*  
525 **2016**, *4*, 744–750.
- 526 (47) Zhao, S.; Dong, B.; Ge, R.; Wang, C.; Song, X.; Ma, W.; Wang, Y.; Hao, C.; Guo, X.;  
527 Gao, Y. Channel-wall functionalization in covalent organic frameworks for the enhance-  
528 ment of CO<sub>2</sub> uptake and CO<sub>2</sub>/N<sub>2</sub> selectivity. *RSC Advances* **2016**, *6*, 38774–38781.
- 529 (48) van der Jagt, R.; Vasileiadis, A.; Veldhuizen, H.; Shao, P.; Feng, X.; Ganapathy, S.;  
530 Habisreutinger, N. C.; van der Veen, M. A.; Wang, C.; Wagemaker, M.; van der  
531 Zwaag, S.; Nagai, A. Synthesis and Structure–Property Relationships of Polyimide  
532 Covalent Organic Frameworks for Carbon Dioxide Capture and (Aqueous) Sodium-Ion  
533 Batteries. *Chemistry of Materials* **2021**, *33*, 818–833.
- 534 (49) Wang, J.-C.; Kan, X.; Shang, J.-Y.; Qiao, H.; Dong, Y.-B. Catalytic asymmetric synthesis  
535 of chiral covalent organic frameworks from prochiral monomers for heterogeneous  
536 asymmetric catalysis. *J. Am. Chem. Soc.* **2020**, *142*, 16915–16920.

- 537 (50) Gropp, C.; Ma, T.; Hanikel, N.; Yaghi, O. M. Design of higher valency in covalent  
538 organic frameworks. *Science* **2020**, *370*, eabd6406.
- 539 (51) Wang, X.; Han, X.; Zhang, J.; Wu, X.; Liu, Y.; Cui, Y. Homochiral 2D porous covalent  
540 organic frameworks for heterogeneous asymmetric catalysis. *J. Am. Chem. Soc.* **2016**,  
541 *138*, 12332–12335.
- 542 (52) Zhao, C.; Lyu, H.; Ji, Z.; Zhu, C.; Yaghi, O. M. Ester-linked crystalline covalent organic  
543 frameworks. *J. Am. Chem. Soc.* **2020**, *142*, 14450–14454.
- 544 (53) Thomas, S.; Li, H.; Zhong, C.; Matsumoto, M.; Dichtel, W. R.; Bredas, J.-L. Electronic  
545 Structure of Two-Dimensional  $\pi$ -Conjugated Covalent Organic Frameworks. *Chemistry*  
546 *of Materials* **2019**, *31*, 3051–3065.
- 547 (54) Er, D.; Dong, L.; Shenoy, V. B. Mechanisms for Engineering Highly Anisotropic Con-  
548 ductivity in a Layered Covalent-Organic Framework. *The Journal of Physical Chemistry*  
549 *C* **2015**, *120*, 174–178.
- 550 (55) Wang, M. et al. Unveiling Electronic Properties in Metal-Phthalocyanine-Based Pyrazine-  
551 Linked Conjugated Two-Dimensional Covalent Organic Frameworks. *Journal of the*  
552 *American Chemical Society* **2019**, *141*, 16810–16816.
- 553 (56) Li, Y.; Liu, M.; Wu, J.; Li, J.; Yu, X.; Zhang, Q. Highly stable  $\beta$ -ketoenamine-based  
554 covalent organic frameworks (COFs): synthesis and optoelectrical applications. *Frontiers*  
555 *of Optoelectronics* **2022**, *15*.
- 556 (57) Kim, Y. H.; Kim, N.; Seo, J.-M.; Jeon, J.-P.; Noh, H.-J.; Kweon, D. H.; Ryu, J.; Baek, J.-  
557 B. Benzothiazole-Based Covalent Organic Frameworks with Different Symmetrical  
558 Combinations for Photocatalytic CO<sub>2</sub> Conversion. *Chemistry of Materials* **2021**, *33*,  
559 8705–8711.

- 560 (58) Peng, L.; Chang, S.; Liu, Z.; Fu, Y.; Ma, R.; Lu, X.; Zhang, F.; Zhu, W.; Kong, L.;  
561 Fan, M. Visible-light-driven photocatalytic CO<sub>2</sub> reduction over ketoenamine-based  
562 covalent organic frameworks: role of the host functional groups. *Catalysis Science &*  
563 *Technology* **2021**, *11*, 1717–1724.
- 564 (59) Vyas, V. S.; Haase, F.; Stegbauer, L.; Savasci, G.; Podjaski, F.; Ochsenfeld, C.;  
565 Lotsch, B. V. A tunable azine covalent organic framework platform for visible light-  
566 induced hydrogen generation. *Nat. Commun.* **2015**, *6*, 8508.
- 567 (60) Zoubritzky, L.; Coudert, F.-X. CrystalNets.jl: Identification of Crystal Topologies.  
568 *SciPost Chemistry* **2022**, *1*.
- 569 (61) Stegbauer, L.; Schwinghammer, K.; Lotsch, B. V. A hydrazone-based covalent organic  
570 framework for photocatalytic hydrogen production. *Chem. Sci.* **2014**, *5*, 2789–2793.
- 571 (62) Yang, J. et al. Protonated Imine-Linked Covalent Organic Frameworks for Photocatalytic  
572 Hydrogen Evolution. *Angewandte Chemie International Edition* **2021**, *60*, 19797–19803.
- 573 (63) Hamad, S.; Hernandez, N. C.; Aziz, A.; Ruiz-Salvador, A. R.; Calero, S.; Grau-Crespo, R.  
574 Electronic structure of porphyrin-based metal–organic frameworks and their suitability  
575 for solar fuel production photocatalysis. *Journal of Materials Chemistry A* **2015**, *3*,  
576 23458–23465.
- 577 (64) Huber, S. P. et al. AiiDA 1.0, a scalable computational infrastructure for automated  
578 reproducible workflows and data provenance. *Scientific Data* **2020**, *7*.
- 579 (65) Uhrin, M.; Huber, S. P.; Yu, J.; Marzari, N.; Pizzi, G. Workflows in AiiDA: Engineering  
580 a high-throughput, event-based engine for robust and modular computational workflows.  
581 *Computational Materials Science* **2021**, *187*, 110086.
- 582 (66) Cube analysis. <https://github.com/kjappelbaum/cubes>, Accessed: 2022-09-17.

- 583 (67) Ganose, A. M.; Jackson, A. J.; Scanlon, D. O. sumo: Command-line tools for plotting  
584 and analysis of periodic *ab initio* calculations. *Journal of Open Source Software* **2018**,  
585 *3*, 717.
- 586 (68) Groom, C. R.; Bruno, I. J.; Lightfoot, M. P.; Ward, S. C. The Cambridge structural  
587 database. *Acta Crystallogr. B: Struct. Sci. Cryst. Eng. Mater.* **2016**, *72*, 171–179.
- 588 (69) Ehrt, C.; Krause, B.; Schmidt, R.; Ehmki, E. S. R.; Rarey, M. SMARTS.plus – A  
589 Toolbox for Chemical Pattern Design. *Molecular Informatics* **2020**, *39*, 2000216.
- 590 (70) Ho, J.; Tumkaya, T.; Aryal, S.; Choi, H.; Claridge-Chang, A. Moving beyond P values:  
591 data analysis with estimation graphics. *Nature Methods* **2019**, *16*, 565–566.

592 **TOC Graphic**

593

